

---

# D<sup>2</sup>B: Deep Distribution Bound for Natural-looking Adversarial Attack

---

**Qiuling Xu**

Department of Computer Science  
Purdue University  
xu1230@purdue.edu

**Guanhong Tao**

Department of Computer Science  
Purdue University  
taog@purdue.edu

**Xiangyu Zhang**

Department of Computer Science  
Purdue University  
xyzhang@cs.purdue.edu

## Abstract

We propose a novel technique that can generate natural-looking adversarial examples by bounding the variations induced for internal activation values in some deep layer(s), through a distribution quantile bound and a polynomial barrier loss function. By bounding model internals instead of individual pixels, our attack admits perturbations closely coupled with the existing features of the original input, allowing the generated examples to be natural-looking while having diverse and often substantial pixel distances from the original input. Enforcing per-neuron distribution quantile bounds allows addressing the non-uniformity of internal activation values. Our evaluation on ImageNet and five different model architecture demonstrates that our attack is quite effective. Compared to the state-of-the-art pixel space attack, semantic attack, and feature space attack, our attack can achieve the same attack success/confidence level while having much more natural-looking adversarial perturbations. These perturbations piggy-back on existing local features and do not have any fixed pixel bounds.

## 1 Introduction

Adversarial attack is a prominent security threat for Deep Learning (DL) applications. Given a legal input, perturbation is applied to the input to derive an adversarial example, which causes the DL model to misclassify. The perturbation is usually small, e.g.,  $[-4, 4]$  in the RGB range of  $[0, 255]$ , such that it is imperceptible by humans. Depending on the methods to generate such adversarial examples, there are *white-box* attacks, such as PGD [1], C&W [2], BIM [3], and FGSM [4], which assume access to model internals and leverage gradient information in sample generation, and *black-box* attacks, such as ZOO [5] and boundary attack [6], that assume no access to model internals and directly mutate inputs based on classification outputs. Our work falls into the *white-box* attack category in the image classification domain. The perturbation bounds are critical for adversarial attack because a large bound usually implies high attack success rate but a less natural-looking example. The second and third columns of Figure 1 show a number of samples with a small bound (i.e.,  $\ell_\infty = 5/255$ , meaning the maximum pixel value change is 5 out of 255) and a larger bound (i.e.,  $\ell_\infty = 16/255$ ) for the BIM attack<sup>1</sup>. Observe that with the larger bound, the adversarial perturbation is detectable by human eyes. As such, it is often assumed that adversarial perturbation has a small bound. The success of a large

<sup>1</sup>We use BIM instead of other pixel space attacks such as PGD because we found that (compared to BIM) the random initialization of PGD degrades imperceptibility at a non-trivial scale, in exchange for just a slightly higher success rate. Hence, we consider BIM a more compelling baseline as we stress imperceptibility.

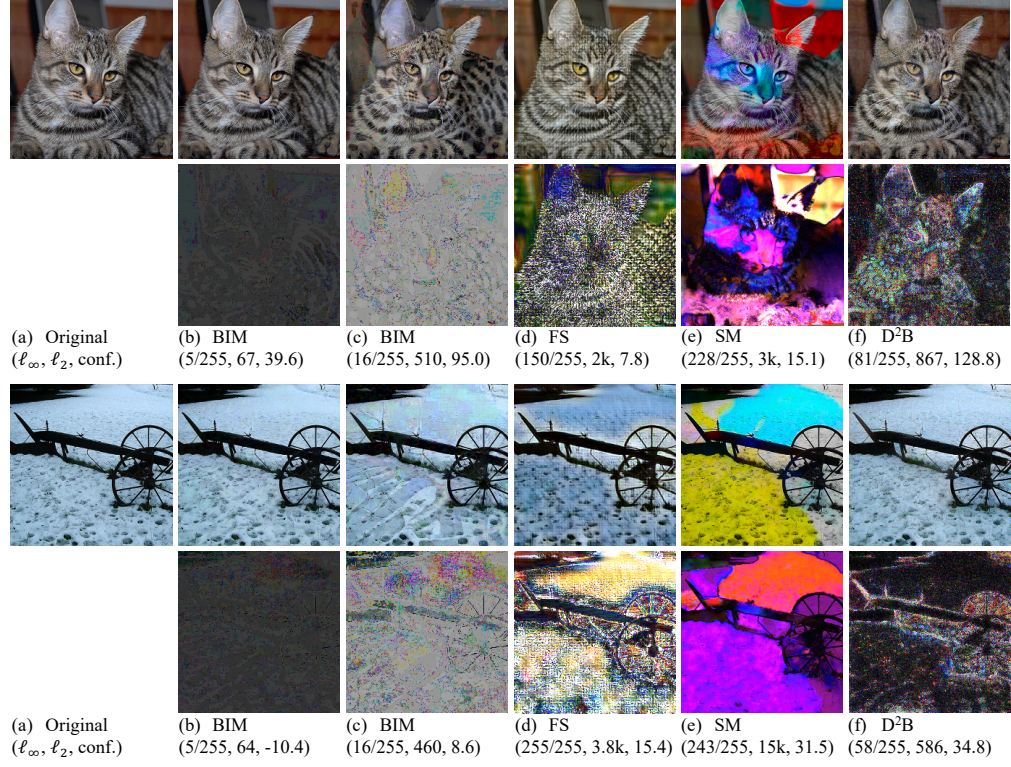


Figure 1: Adversarial examples of different attacks/attack-settings. The first column represents the original images. The second and third columns shows examples from Basic Iterative Method (BIM) with a small and a large pixel distances, respectively. The following columns are samples from Feature Space Attack(FS), Semantic Attack (SM) and our Deep Distribution Bounded Attack ( $D^2B$ ). For each set of images, the first row presents the adversarial examples. The second row shows the perturbations applied to the original image. We enlarge the perturbations of BIM by 10 times and the others' by 5 times for better illustration. On the bottom of each column, there is a triple representing the  $\ell_\infty$ ,  $\ell_2$  distances and the attack confidence of each example. A positive value indicates the attack yielded misclassification and a large value indicates the model is very confident about the (misclassification) result.

number of existing defense, verification, and validation techniques [1, 3, 7–17] are based on such assumption. For example, given a particular input and a small bound, many techniques aim to prove that a model must not misclassify for any perturbation within the bound [13–15, 18].

Recently, researchers have shown that adversarial examples with large pixel distances (from the original inputs) can be generated. Such distances are usually way beyond the bounds that many existing defense and validation techniques aim to protect, providing a new attack vector. Specifically, *semantic attack* [19] manipulates the color and texture of a benign image, through a specifically modified colorization model and a texture transfer method. *Feature space attack* [20] leverages *style transfer* [21] to mutate the (implicit) styles of normal inputs to derive adversarial examples. In particular, it perturbs the distribution (e.g., mean and variation) of internal feature map to inject malicious and largely human-imperceptible style differences that lead to misclassification. The third and fourth columns in Figure 1 show some examples for feature attack and semantic attack, respectively. Observe that they have much larger  $\ell_\infty$  and  $\ell_2$  distances (from the original inputs in the first column) than the examples generated by BIM attacks. While they are in general more natural-looking compared to examples generated by pixel space attacks with a similar distance, the perturbations are quite noticeable in human eyes. This is confirmed by our human study (Section 4.1), in which we show that with a 80% attack success rate, humans can clearly recognize the adversarial examples. The root cause is that these techniques focus on mutating *meta features* of original inputs, such as colors and styles, due to the difficulty of harnessing perturbations on *content features*, such as shapes and local patterns. However, a successful semantic/feature attack may still entail substantial meta feature mutation, degrading the attack's stealthiness. More discussion on related work can be found in Section 2.

In this paper, we propose a novel adversarial attack that can perform stealthy content feature mutation. The last column of Figure 1 shows the examples generated by our technique and its pixel level contrast with the original image. Observe that the differences largely piggy back on the content features of the original example (by having similar shapes and local content patterns as the original inputs), making them human imperceptible. In comparison, the differences of the examples generated by semantic and feature space attacks are more pervasive and global. For example, the feature space attack on the cat image induces a global checkerboard style, while our attack induces perturbations that reside as part of the local features of the cat. The semantic attack on the barrow image below generates visible color blocks, while our attack induces more perturbations for places that have intensive local features and less perturbations for those with disperse local features such as the snowy background. According to our human study in Section 4.1, our technique can achieve 95% attack success rate and yet humans cannot easily distinguish the adversarial examples from the benign ones.

The essence of our technique is to bound internal activation changes instead of bounding the pixel space changes like many existing techniques. Assuming internal neurons represent implicit features, particularly content features, small perturbations to the activations of these neurons denote small variations of the corresponding features. However, we find it challenging to properly control internal perturbations. A naive method of limiting the variation of activation values after ReLU function to a range does not work and leads to abrupt pixel space perturbations that are human visible. The reason is that a small activation change after ReLU may entail substantial value change before the ReLU and eventually human perceptible pixel mutations in the input space. Moreover, while in the pixel space, a perturbation value range has consistent meaning/effect across multiple pixels, an internal value perturbation range does not possess such consistency across multiple neurons. For instance, small activation changes may significantly affect classification result and entail substantial pixel space changes (in order to achieve such inner differences) for some neurons, while activation changes with an orders-of-magnitude larger scale may have very little effect for some other neurons. These pose new challenges to the underlying optimization methods.

In order to address these challenges, we propose the following solutions. Given a model, its internal structure is inspected to select a place whose inner values roughly follow normal distributions. We call it a *throttle plane*, which is a notion with finer granularity than a layer in deep learning model. Intuitively, consider that a layer consists of many operations, such as matrix multiplication, vector additions, and application of activation functions. A throttle plane is defined by one of such operations in a layer. ReLU functions are not good candidates for throttle planes as the activation value distributions for individual neurons (over all training samples) usually do not follow a normal distribution (see Section 3.1). After identifying the throttle plane, for each neuron on the plane, we collect its inner value distribution over the training set. Such distributions allow us to provide *neuron-specific* bounds during perturbation. These bounds are defined based on the normal distributions (e.g., 10% quantile change). We then enforce the bound using a *polynomial internal barrier loss* (Section 3.2). *Barrier method* (BM) [22] is a method developed for constrained optimization problems. Intuitively, it adds substantial penalty through a barrier loss when a value approaches its boundary. By default, BM uses a log-based barrier loss, which is not ideal and has numerical instability problems in our context. We hence develop a polynomial loss function. We conduct experiments on ImageNet and five models, including both naturally and adversarially trained models. Comparative experiments with state-of-the-art pixel-space/feature/semantic attacks show that our attack produces adversarial examples that are much more natural-looking when achieving the same level of attack conference/success-rate. Further evaluation against three different detection techniques demonstrates that our attack has better/comparable persistence compared to other attacks while having better imperceptibility, due to the new vulnerable aspects it attacks.

## 2 Other Related Work

In addition to the aforementioned works, Song et al. [23] considered generating unbounded adversarial examples through GAN-based method. Hosseini and Poovendran [24] and Laidlaw and Feizi [25] proposed to uniformly change the color and the lightning condition to construct adversarial examples. In comparison, D<sup>2</sup>B attacks local content features. Kumari et al. [26] applied  $\ell_\infty$  bounded perturbation on internal activation to strengthen the effect of adversarial training. It leveraged a two-step optimization method. However, its internal bound is uniform. We show in Appendix 6.2 that their optimization is not effective for our purpose. Xie et al. [27] proposed to denoise internal activation

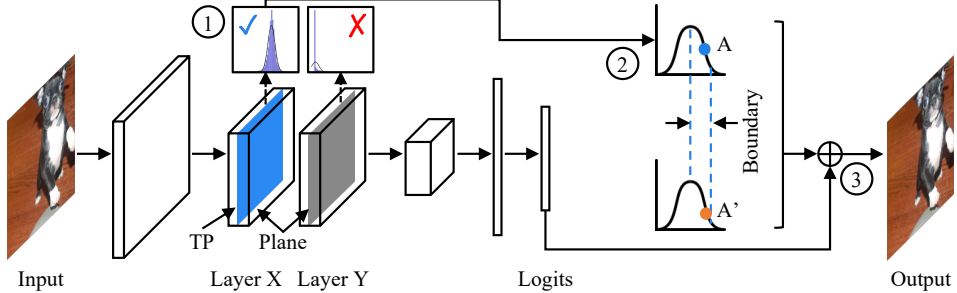


Figure 2: Workflow of our attack. It consists of three steps: ① throttle plane (TP) selection, ② internal distribution boundary constraint, and ③ adversarial sample generation with combined losses. for better adversarial training. Inkawich et al. [28] found simulating the feature representation of target images can increase attack transferability.

### 3 Attack Design

Figure 2 describes the workflow of our attack. Given a target model and its training set, we first perform throttle plane (TP) selection (step ①). Specifically, we run the target model over the training dataset and collect the inner value distributions at the end of individual operations along the forward data path (e.g., multiplication with a kernel matrix). The values for the same operation across all neurons and channels form a plane (e.g., the blue and gray planes in Figure 2). Note that since a layer may consist of multiple operations, it may have multiple planes. A plane whose value distribution has a normal distribution is a possible throttle plane (TP) to harness the adversarial perturbation (e.g., the blue plane in Figure 2). With a (or multiple) selected throttle plane(s), we further inspect the possible distribution boundary for each neuron at step ②. That is, the perturbed value  $A'$  should be bounded within some distribution quantile range of the original value  $A$ . Finally, we model the constraint of distribution boundary by an internal barrier loss function, which is combined with the cross-entropy prediction loss. During attack (step ③), a normal input is fed to the model and updated with respect to the combined attack loss, which produces a successful natural-looking adversarial example.

#### 3.1 Distribution based Bounding and Throttle Plane Selection

The overarching design of our attack is to harness perturbation at the selected *throttle plane(s)* such that only small variations of abstract features are allowed. Note that the corresponding pixel space perturbations could be substantial as long as the inner value changes are within bound. Identifying appropriate throttle plane(s) is the first challenge we need to address. Intuitively, if we consider model execution as horizontal data flow from the input space to the output space, *a plane contains the values lie in a vertical cut of the data flow*. The cut could lie in the border between layers or even in between operations within a layer. Formally, *a plane consists of all the values right after an operation along the data flow from the input space to the output space across all the neurons/channels*. As such, the input values and the output values form planes; the activation values right after the activation function of a layer form a plane too.

**Challenges of Having Internal Throttle Plane.** Traditional adversarial sample generation techniques simply place the perturbation throttle at the input plane. This makes the design simple as the perturbation happens exactly within the throttle plane. In contrast, placing the throttle in an inner plane poses new challenges.

First of all, while in the input space values have uniform semantics (e.g., denoting the RGB values of individual pixels), values in the inner space do not have such property. The different values on the same inner plane often denote different abstract features whose value ranges have diverse semantics. As such, a uniform perturbation bound across all these internal values is meaningless. Second, in our design, the perturbation occurs in the input space while the throttle is placed somewhere inside the model. Hence, the perturbation is not directly controlled and could be substantial. An important hypothesis is that since the perturbations can only induce bounded inner value changes at the throttle plane, they denote small semantic mutations of the abstract features. However, given a particular inner value, the semantic mutation entailed by its changes is non-uniform within its range. Consider Figure 3 (b), which denotes the distribution of an inner value (across the training set). Observe that

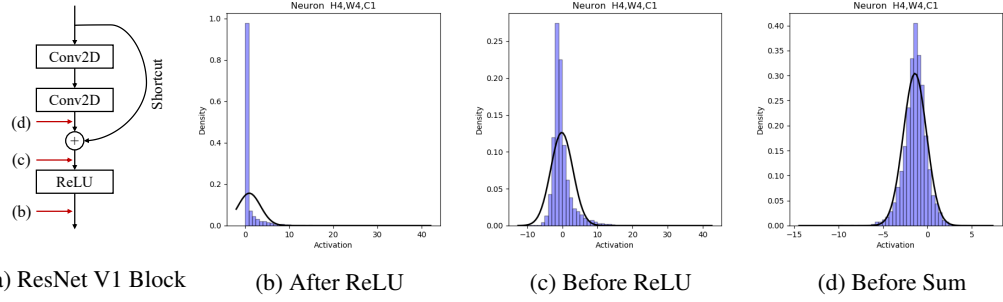


Figure 3: Operations in the last block of group 4 of an adversarially trained ResNet152 and typical distribution of some value on different planes

variation of 1 when the value is 2 implies much more substantial semantic changes (indicated by the entailed substantial quantile change) than when the value is 20, which is at the very tail of the distribution, as the model is likely insensitive to such a large value.

**Our Design – Looking for Normal Distributions.** According to the above discussion, we cannot utilize a uniform bound across the different inner values (on the plane); we cannot utilize the same bound even when the value varies (from one input to another). Therefore, we propose a novel idea of utilizing distribution based bounds. Particularly, we collect the distributions for the individual values (on the plane). During perturbation, the bound for each inner value is based on its distribution. As such, not only different values along the plane have different bounds, but also the value may have different bound when it varies from input to input. In particular, we *select the plane(s) whose values have normal distributions*, which allows us to have precise and relatively easy control of the level of semantic mutation allowed, *by using a quantile bound based on the current value and its distribution*, instead of using a concrete value bound. In the following, we use a few examples to illustrate the reasons of looking for inner throttle plane with normal distributions.

Take a block of an adversarially trained ResNet152 for example (Figure 3 (a)). If we set the throttle plane at the block boundary (i.e., right after the ReLU function), the distribution for some value on the plane (across the entire training set) is shown in Figure 3 (b). Observe that while the distribution is dense on the positive side, the negative side is vacant (due to ReLU). It is hence not a good choice for throttle plane. The reason is that we completely lose control on the negative side. Intuitively, substantial input perturbations would be admitted as long as they do not cause the inner value to flip from negative to positive after ReLU. This would substantially degenerate the naturalness of the generated adversarial samples (see Figure 4(b) for an example). If we set the plane right before ReLU, according to Figure 3 (c), it is a skewed distribution. By inspecting the block structure, we find that the value is the sum of the shortcut and the main output (please refer to [29] for the explanation of these terms of ResNet structure). The skew is mainly due to the shortcut. It creates difficulty for enforcing a quantile bound as it is hard to have a general way of modeling such distribution. Figure 4(c) shows an adversarial example generated by putting the throttle at this plane. Observe that it is not natural either. We further inspect the plane right before the sum operation. Figure 3 (d) shows one of the distributions. Observe that it can be modeled as a normal distribution. Bounding this plane leads to a natural-looking adversarial Figure 4(d)<sup>2</sup>. Figure 12(e) in Appendix 6.10 shows the distributions for a set of randomly selected values on the same plane. Observe they approximately follow normal distributions. Also observe that their distribution parameters are quite different, supporting our design of using different bounds for various values on a plane.

Upon sample generation, given a benign input, the inner values on the selected throttle plane(s) are collected. The bound of a value is then determined by its quantile of the value (on its density function). How to enforce such quantile bounds is discussed in the following section.

### 3.2 Enforcing Quantile Bound with Polynomial Barrier Loss

Let  $\mathcal{D}$  be a distribution on support  $\mathcal{S}$ . The activation  $y_i$  of neuron  $i$  on a selected throttle plane  $\mathcal{I}$  is a random variable through mapping  $f_i : \mathcal{S} \rightarrow \mathbb{R}$ ,  $y_i \sim f_i(\mathcal{D})$ . We denote the cumulative distribution

<sup>2</sup>In this case, we also bound another throttle plane to control the values along the shortcut. The two throttle planes together form a complete cut of the forward dataflow.



(a) Original (b) After ReLU (c) Before ReLU (d) Before Sum

Figure 4: Adversarial images when the throttle plane is placed at different positions in the last block of group 4 of an adversarially trained Resnet-152 model, under the same perturbation bound.

function of  $y_i$  as  $C_i(x)$ , and the corresponding quantile function as  $C_i^{-1}$ . Let the original image be  $x^{\text{nat}}$  and the adversarial sample be  $x^{\text{adv}}$ . Correspondingly, let  $y_i^{\text{adv}}$  and  $y_i^{\text{nat}}$  be the respective activations from  $x^{\text{nat}}$  and  $x^{\text{adv}}$ . Assume the allowed quantile change is less than a threshold  $\epsilon$ . The corresponding value bound for  $y_i^{\text{adv}} \in [\text{low}_i, \text{high}_i]$ , is hence  $[C_i(C_i^{-1}(x^{\text{nat}}) - \epsilon), C_i(C_i^{-1}(x^{\text{nat}}) + \epsilon)]$ . Note that we translate the quantile bound to a value bound, over which we can define a loss function.

**Polynomial Barrier Loss.** *Interior point method* or *barrier method* [22] is a standard technique for constrained optimization. It is widely used in linear programming applications [30]. It utilizes a negative log function in the loss function by default. However, it was intended to be used in problems where the bound is hard, meaning the values must not exceed the bound as the loss becomes infinitely large when the value infinitely approaches the bounds. In our context, a hard bound does not work well with ReLU functions. Specifically, input changes guided by gradients may activate some previously inactive neurons, leading to the inner values to exceed their bounds, causing numerical exceptions (on the log function). Another naive design is to introduce a ReLU kind of bound, that is, the loss is 0 while the value is in bound and some large value otherwise. However, such a design does not apply penalty when the value is approaching the bound.

Therefore, we devise a polynomial barrier loss function as follows.

$$\mathcal{L}_i(y_i^{\text{adv}}) = k \left[ \frac{\text{ReLU}(y_i^{\text{adv}} - y_i^{\text{nat}})}{\text{high}_i - y_i^{\text{nat}}} + \frac{\text{ReLU}(y_i^{\text{nat}} - y_i^{\text{adv}})}{y_i^{\text{nat}} - \text{low}_i} \right]^b$$

We empirically set  $k = 1e5$  and  $b = 200$ . Intuitively, the loss function applies an extremely large penalty (by the power  $b = 200$ ) when the inner value induced by adversarial perturbation is beyond the bound. When the value is within the bound and close to the boundary values, measured by the two fractions, a large penalty is applied, discouraging the value from going beyond. For example, when  $y_i^{\text{adv}}$  is larger than  $y_i^{\text{nat}}$  and close to the upper bound  $\text{high}$ , say  $\frac{\text{ReLU}(y_i^{\text{adv}} - y_i^{\text{nat}})}{\text{high} - y_i^{\text{nat}}} = 0.99$ , the loss is  $1e5 \times 0.99^{200} \approx 1e4$ . We have also tried a linear barrier loss, which cannot effectively enforce the bound. Please refer to Appendix 6.1 for detailed discussion.

**Optimization Method.** With the polynomial barrier loss, we use a regular gradient sign method [2] for optimization. There are other design choices. For example, in [26], a two-step optimization was proposed to facilitate adversarial example generation by leveraging internal values. Specifically, it first perturbs the internal values at some inner layer to induce misclassification and then it uses a mean squared error loss to optimize the input to achieve the optimized inner values. However, we found that the method is not that effective when a strict internal boundary is enforced. The reason is that the first step of inner layer optimization tends to find local minimals that are infeasible for input optimization due to the strong correlations across inner values. In contrast, our method directly optimizes at the input space. Another simple method is clipping, which clips the inner values (on a throttle plane) and prevents gradient propagation if they are beyond bounds. Our experience shows that such a simple method can hardly work either. We conduct an experiment to compare the three methods. Our method can better enforce the internal bound and generate adversarial examples with one order of magnitude smaller average boundary size. Details can be found in Appendix 6.2. How to identify the appropriate learning rate is discussed in Appendix 6.5. In some rare cases, the generated examples may have checkerboard patterns. We use an additional feature smoothing step to mitigate such effects. Details can be found in Appendix 6.3.

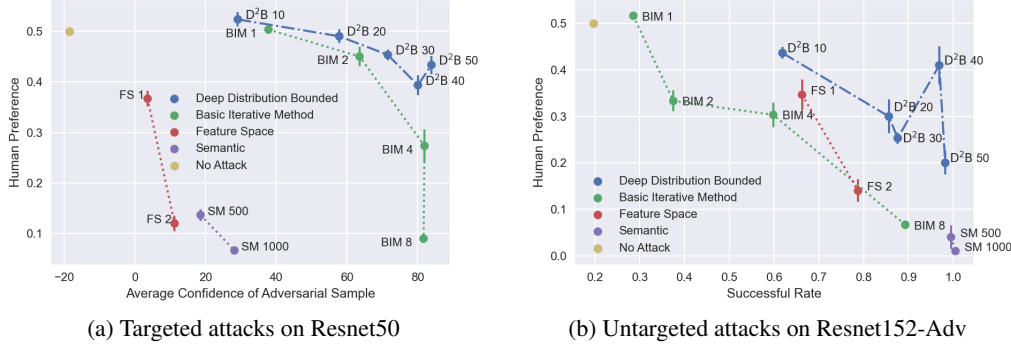


Figure 5: Quality of generated adversarial examples. In (a) the targeted attack, the  $x$  axis represents the average confidence of adversarial examples, where a confidence value indicates the level of success of the attack with a greater than 0 value meaning the model misclassifies to the target label. The  $y$  axis denotes the rate that humans consider the adversarial examples real (compared to the benign images), with 50% meaning humans cannot distinguish an adversarial example from its benign version. In (b) the untargeted attacks against the adversarially trained ResNet152, we use the attack success rate as the  $x$  axis. Note that we cannot use attack success rate in the targeted attacks as all those attacks have close to 100% success rate because the model was normally trained. The  $y$  axis is the same as in (a). We regard an untargeted attack successful if the true label does not appear in the top-5 predicted labels, which is consistent with the literature [27]. The vertical bar on a data point (i.e., an attack setting) represents the standard error of the human preference rate.

Table 1: Pixel and quantile distances for ResNet50, with Conf. meaning attack confidence

Attack	Conf.	Pixel Dist.		$\ell_\infty$ Quantile Dist.		
		$\ell_2$	$\ell_\infty$	Plane 1	Plane 2	Plane 3
BIM4	81.91	10.81	0.04	0.62	0.83	0.90
D <sup>2</sup> B10	30.29	4.26	0.07	0.06	0.08	0.09
D <sup>2</sup> B20	58.82	6.27	0.09	0.12	0.16	0.17
D <sup>2</sup> B30	72.43	7.28	0.10	0.18	0.24	0.26
D <sup>2</sup> B40	80.06	7.88	0.11	0.24	0.32	0.35
D <sup>2</sup> B50	84.52	8.25	0.11	0.30	0.41	0.44

Table 2: Pixel and quantile distances for ResNet152-Adv, with Succ. meaning attack success rate

Attack	Succ.	Pixel Dist.		$\ell_\infty$ Quantile Dist.		
		$\ell_2$	$\ell_\infty$	Plane 1	Plane 2	Plane 3
BIM4	0.58	14.49	0.04	0.65	0.82	0.89
D <sup>2</sup> B10	0.61	6.65	0.11	0.06	0.08	0.09
D <sup>2</sup> B20	0.86	15.43	0.24	0.13	0.16	0.17
D <sup>2</sup> B30	0.86	16.68	0.19	0.19	0.24	0.26
D <sup>2</sup> B40	0.97	21.84	0.22	0.26	0.33	0.35
D <sup>2</sup> B50	0.98	27.08	0.26	0.33	0.41	0.44

## 4 Experiments

To evaluate our attack and the quality of generated adversarial examples, we conduct experiments on one of the largest image datasets, ImageNet [31]. We use five types of DNN models in the evaluation and compare the quality of our generated adversarial examples with three existing attack methods. Finally, we evaluate our attack on three popular adversarial detection approaches.

### 4.1 Visual Quality of Generated Examples

In this section, we evaluate the visual quality of generated adversarial examples by our attack. We also compare our technique with three existing attack methods: BIM [3], feature space attack [20] and semantic attack [19]. We use these four attack methods to generate adversarial examples for a naturally trained ResNet50 model [32] and an adversarially trained ResNet152 model [33] (ResNet152-adv), respectively. For BIM, feature space attack and our attack, we stop the attack optimization when convergence is reached (no confidence increase). For semantic attack, we use a preset number of optimization steps. Note that it is unbounded and the optimization step controls the perturbation and the attack success rate. Details about throttle planes used are discussed in Appendix 6.7.

In order to measure the naturalness of generated examples, we perform a human study using Amazon Turk. We employ a similar setting as that in [34]. Specifically, for each attack setting, users are given

100 pairs of images, each consisting of a real image and its adversarial counterpart. They are asked to choose the one that looks real. Each user is given 5 test-drives before the study starts. Each pair of image appears on screen for 5 seconds and is evaluated by three different users. The experiment is performed for each attack setting. There are totally 26 settings (for the four attacks) and 156 users participated in our study. 155 out of the 156 responses are considered valid, with those deviating far from the majority (exceeding two times of the standard deviation) removed. We post all the examples used in human study online [35].

Figure 5 shows the results.  $BIMx$  denotes the Basic Iterative Method [3] with an  $\ell_\infty$  bound  $x\%$  of 255. For example,  $BIM4$  means the  $\ell_\infty$  bound is  $255 \times 4\% \approx 11$ . Feature space attack selects an internal layer and then performs bounded perturbation of the mean and variance of the feature maps at that layer [20].  $FS1$  and  $FS2$  are feature space attacks using the  $relu2\_1$  and  $relu3\_1$  layers of VGG16, respectively, as the perturbation layers.  $SMx$  is semantic attack with an optimization step of  $x$  and the number of clusters set to 8 [19]. For our attack, we use the average observed internal value  $\ell_\infty$  quantile change (at a throttle plane) for the adversarial examples by  $BIM4$  as a reference.  $D^2Bx$  denotes that we allow  $x\%$  of the average quantile change observed in  $BIM4$  at the throttle plane. Figure 5a shows the results for targeted attacks on the naturally trained ResNet50 and Figure 5b for untargeted attacks on the adversarially trained ResNet152. We can see that our attack has the highest attack confidence/success rate at the same level of human preference; and given a same confidence/success rate, our adversarial examples are consistently more favored by the testers (for being more natural-looking), compared to those by other attacks. Our adversarial examples with the most aggressive settings (e.g.,  $D^2B40$  and  $D^2B50$ ) have similar human preference to pixel space attack with a very small bound ( $BIM2$  and  $BIM4$ ), indicating our attack is indeed imperceptible. With the increase of quantile change, perturbation bound, or optimization step, all the attacks achieve a higher success rate, and our attack is increasingly more imperceptible than others. We further study the pixel distance and quantile distance of the generated adversarial examples by different attacks. Table 1 and Table 2 show that with a similar level of attack confidence or attack success rate, our attack has smaller  $\ell_2$  pixel distance and  $\ell_\infty$  quantile distance. This indicates that our generated examples can achieve a similar level of attack effectiveness with less perturbation, and they are hence more natural-looking. In other words, it can tolerate more aggressive perturbation without degrading naturalness as much, demonstrating the benefits of bounding deep layers. The larger  $\ell_\infty$  pixel distance and the smaller  $\ell_2$  pixel distance (compared to  $BIM4$ ) indicate our perturbations are more diverse, heavily piggy-backing on original features. The attack effectiveness and pixel/internal distances for other models are similar. Details can be found in Appendix 6.8. More adversarial examples generated by the different settings of our attack can be found in Figure 9 and Figure 10 in Appendix 6.9. We also conduct a study about the essence of  $D^2B$  by studying the places that it aims to attack. Details can be found in Appendix 6.6.

## 4.2 Evaluation Against Detection Approaches

We evaluate  $D^2B$  against three popular detection approaches: feature squeezing [36], JPEG [37], and Hu et al. [38]. We generate 100 adversarial examples for each of these approaches. For feature squeezing, we use the same settings as in the original paper [36]. For JPEG [37], we compress the image with 75 quality. For Hu et al. [38], we use 30 examples for fine-tuning the threshold and the remaining 70 for testing. We compare with three existing attack methods:  $BIM$  [3] ( $BIM4$ ), feature space attack [20] ( $FS1$ ) and semantic attack [19] ( $SM50$ ), whose settings were discussed in Section 4.1. For all the attacks, we generate untargeted adversarial examples against the adversarially trained ResNet152 and targeted examples against the naturally trained ResNet50, without knowing the existence of detection methods (i.e., not adaptive). Table 3 and Table 4 show the results. The three columns for feature squeezing are the results for different defense settings. We can observe that our untargeted attack  $D^2B40$  has the highest human preference. In the meantime, it achieves better success rates than the other attacks for feature squeezing and JPEG; and comparable (and high) attack success rates for Hu et al. [38]. Recall that these attacks are on an adversarially trained model and hence the detection techniques may not be able to add much, especially for our attack that closely couples perturbation with existing features. Similarly for the targeted attacks, with a clearly better human preference rates, our attack is more or comparably persistent in the presence of detection. Note that since this is a normally trained model, some detection techniques such as feature squeezing may provide very good defense. Observe that our human preference rates in both scenarios are high, indicating that our attack may potentially conduct more aggressive perturbation to

Table 3: Untargeted attacks on the adversarially trained ResNet152-Adv and detection, with Pref. meaning human preference

Attack	Feature Squeezing			JPEG	Hu et al. [38]	Pref.
	2x2	11-3-4	5-bit			
BIM4	50/100	55/100	57/100	57/100	48/70	30%
FS1	46/100	46/100	46/100	48/100	<b>48/70</b>	35%
SM50	51/100	51/100	60/100	60/100	44/70	29%
D <sup>2</sup> B40	<b>79/100</b>	<b>97/100</b>	<b>99/100</b>	<b>64/100</b>	46/70	<b>41%</b>

Table 4: Targeted attacks on ResNet50 and detection, with Pref. human preference

Attack	Feature Squeezing			JPEG	Hu et al. [38]	Pref.
	2x2	11-3-4	5-bit			
BIM4	30/100	<b>91/100</b>	100/100	51/100	46/70	27%
FS1	6/100	25/100	53/100	24/100	<b>65/70</b>	36%
SM50	0/100	4/100	10/100	1/100	49/70	21%
SM500	5/100	72/100	95/100	46/100	48/70	14%
D <sup>2</sup> B100	<b>37/100</b>	88/100	<b>100/100</b>	<b>57/100</b>	60/70	<b>50%</b>

evade detection (e.g., through adaptive attack). We want to point out while these detection techniques were not designed to guard against our attack, it is still worthwhile to understand how D<sup>2</sup>B performs in the presence of these techniques. Detection and defense (e.g., adversarial training) specific for our attack will be the future work. We have also conducted a transferability study of our attack. We observe that D<sup>2</sup>B has a comparable/slightly-better transferability than other attacks. Details can be found in Appendix 6.4.

## 5 Conclusion

We propose a novel adversarial attack that can generate natural-looking adversarial examples by bounding model internals. It leverages a per-neuron normal distribution quantile bound and a polynomial barrier loss to handle the non-uniform bounds for internal values. Our evaluation on ImageNet, five models, and comparison with three other state-of-the-art attacks demonstrates that the examples generated by our attack are more natural. It is also more persistent in the presence of various existing detection techniques.

## References

- [1] Aleksander Madry, Aleksandar Makelov, Ludwig Schmidt, Dimitris Tsipras, and Adrian Vladu. Towards deep learning models resistant to adversarial attacks. In *Proceedings of 6th International Conference on Learning Representations (ICLR)*, 2018.
- [2] Nicholas Carlini and David Wagner. Towards evaluating the robustness of neural networks. In *Proceedings of 38th IEEE Symposium on Security and Privacy (SP)*, pages 39–57. IEEE, 2017.
- [3] Alexey Kurakin, Ian Goodfellow, and Samy Bengio. Adversarial machine learning at scale. In *Proceedings of 5th International Conference on Learning Representations (ICLR)*, 2017.
- [4] Ian J Goodfellow, Jonathon Shlens, and Christian Szegedy. Explaining and Harnessing Adversarial Examples. *arXiv preprint arXiv:1412.6572*, 2014.
- [5] Pin-Yu Chen, Huan Zhang, Yash Sharma, Jinfeng Yi, and Cho-Jui Hsieh. Zoo: Zeroth order optimization based black-box attacks to deep neural networks without training substitute models. In *Proceedings of the 10th ACM Workshop on Artificial Intelligence and Security*, pages 15–26, 2017.
- [6] Wieland Brendel, Jonas Rauber, and Matthias Bethge. Decision-based adversarial attacks: Reliable attacks against black-box machine learning models. In *International Conference on Learning Representations (ICLR)*, 2018.
- [7] Weilin Xu, David Evans, and Yanjun Qi. Feature Squeezing: Detecting Adversarial Examples in Deep Neural Networks. In *Proceedings of the 25nd Annual Network and Distributed System Security Symposium (NDSS)*, 2018.
- [8] Cihang Xie, Jianyu Wang, Zhishuai Zhang, Zhou Ren, and Alan Yuille. Mitigating adversarial effects through randomization. In *International Conference on Learning Representations*, 2018.
- [9] Aditi Raghunathan, Jacob Steinhardt, and Percy Liang. Certified defenses against adversarial examples. In *International Conference on Learning Representations*, 2018.

[10] Florian Tramèr, Alexey Kurakin, Nicolas Papernot, Ian Goodfellow, Dan Boneh, and Patrick McDaniel. Ensemble adversarial training: Attacks and defenses. In *International Conference on Learning Representations*, 2018.

[11] Guanhong Tao, Shiqing Ma, Yingqi Liu, and Xiangyu Zhang. Attacks meet interpretability: Attribute-steered detection of adversarial samples. In *Advances in Neural Information Processing Systems (NeurIPS)*, pages 7717–7728, 2018.

[12] Shiqing Ma, Yingqi Liu, Guanhong Tao, Wen-Chuan Lee, and Xiangyu Zhang. Nic: Detecting adversarial samples with neural network invariant checking. In *Proceedings of 26th Annual Network and Distributed System Security Symposium (NDSS)*, 2019.

[13] Guy Katz, Clark Barrett, David L Dill, Kyle Julian, and Mykel J Kochenderfer. Reluplex: An efficient smt solver for verifying deep neural networks. In *International Conference on Computer Aided Verification*, pages 97–117. Springer, 2017.

[14] Timon Gehr, Matthew Mirman, Dana Drachsler-Cohen, Petar Tsankov, Swarat Chaudhuri, and Martin Vechev. Ai2: Safety and robustness certification of neural networks with abstract interpretation. In *2018 IEEE Symposium on Security and Privacy (SP)*, pages 3–18. IEEE, 2018.

[15] Shiqi Wang, Kexin Pei, Justin Whitehouse, Junfeng Yang, and Suman Jana. Formal security analysis of neural networks using symbolic intervals. In *27th USENIX Security Symposium (USENIX Security)*, pages 1599–1614, 2018.

[16] Mathias Lecuyer, Vaggelis Atlidakis, Roxana Geambasu, Daniel Hsu, and Suman Jana. Certified robustness to adversarial examples with differential privacy. In *2019 IEEE Symposium on Security and Privacy (SP)*, pages 656–672. IEEE, 2019.

[17] Jeremy Cohen, Elan Rosenfeld, and Zico Kolter. Certified adversarial robustness via randomized smoothing. In *International Conference on Machine Learning (ICML)*, pages 1310–1320, 2019.

[18] Mathias Lecuyer, Vaggelis Atlidakis, Roxana Geambasu, Daniel Hsu, and Suman Jana. Certified robustness to adversarial examples with differential privacy. In *Proceedings of 40th IEEE Symposium on Security and Privacy (SP)*, 2019.

[19] Anand Bhattacharjee, Minjin Chong, Kaizhao Liang, Bo Li, and David Forsyth. Unrestricted adversarial examples via semantic manipulation. In *International Conference on Learning Representations (ICLR)*, 2020.

[20] Qiuling Xu, Guanhong Tao, Siyuan Cheng, Lin Tan, and Xiangyu Zhang. Towards feature space adversarial attack. *arXiv preprint arXiv:2004.12385*, 2020.

[21] Xun Huang and Serge Belongie. Arbitrary style transfer in real-time with adaptive instance normalization. In *Proceedings of the IEEE International Conference on Computer Vision (ICCV)*, pages 1501–1510, 2017.

[22] Stephen Boyd, Stephen P Boyd, and Lieven Vandenberghe. *Convex optimization*. Cambridge university press, 2004.

[23] Yang Song, Rui Shu, Nate Kushman, and Stefano Ermon. Constructing unrestricted adversarial examples with generative models. In *Advances in Neural Information Processing Systems*, pages 8312–8323, 2018.

[24] Hossein Hosseini and Radha Poovendran. Semantic adversarial examples. In *Proceedings of the IEEE Conference on Computer Vision and Pattern Recognition Workshops*, pages 1614–1619, 2018.

[25] Cassidy Laidlaw and Soheil Feizi. Functional adversarial attacks. In *Advances in Neural Information Processing Systems*, pages 10408–10418, 2019.

[26] Nupur Kumari, Mayank Singh, Abhishek Sinha, Harshitha Machiraju, Balaji Krishnamurthy, and Vineeth N. Balasubramanian. Harnessing the vulnerability of latent layers in adversarially trained models. In Sarit Kraus, editor, *Proceedings of the Twenty-Eighth International Joint Conference on Artificial Intelligence, IJCAI 2019, Macao, China, August 10-16, 2019*, pages 2779–2785. ijcai.org, 2019. doi: 10.24963/ijcai.2019/385. URL <https://doi.org/10.24963/ijcai.2019/385>.

- [27] Cihang Xie, Yuxin Wu, Laurens van der Maaten, Alan L. Yuille, and Kaiming He. Feature denoising for improving adversarial robustness. In *The IEEE Conference on Computer Vision and Pattern Recognition (CVPR)*, June 2019.
- [28] Nathan Inkawich, Wei Wen, Hai (Helen) Li, and Yiran Chen. Feature space perturbations yield more transferable adversarial examples. In *IEEE Conference on Computer Vision and Pattern Recognition, CVPR 2019, Long Beach, CA, USA, June 16-20, 2019*, pages 7066–7074. Computer Vision Foundation / IEEE, 2019. doi: 10.1109/CVPR.2019.00723. URL [http://openaccess.thecvf.com/content\\_CVPR\\_2019/html/Inkawich\\_Feature\\_Space\\_Perturbations\\_Yield\\_More\\_Transferable\\_Adversarial\\_Examples\\_CVPR\\_2019\\_paper.html](http://openaccess.thecvf.com/content_CVPR_2019/html/Inkawich_Feature_Space_Perturbations_Yield_More_Transferable_Adversarial_Examples_CVPR_2019_paper.html).
- [29] Kaiming He, Xiangyu Zhang, Shaoqing Ren, and Jian Sun. Deep residual learning for image recognition. In *Proceedings of the IEEE Conference on Computer Vision and Pattern Recognition*, pages 770–778, 2016.
- [30] Robert J Vanderbei et al. *Linear programming*. Springer, 2015.
- [31] Olga Russakovsky, Jia Deng, Hao Su, Jonathan Krause, Sanjeev Satheesh, Sean Ma, Zhiheng Huang, Andrej Karpathy, Aditya Khosla, Michael Bernstein, et al. Imagenet large scale visual recognition challenge. *International Journal of Computer Vision*, 115(3):211–252, 2015.
- [32] Kaiming He, Xiangyu Zhang, Shaoqing Ren, and Jian Sun. Deep residual learning for image recognition. *CoRR*, abs/1512.03385, 2015. URL <http://arxiv.org/abs/1512.03385>.
- [33] Cihang Xie, Yuxin Wu, Laurens van der Maaten, Alan L Yuille, and Kaiming He. Feature denoising for improving adversarial robustness. In *Proceedings of the IEEE Conference on Computer Vision and Pattern Recognition (CVPR)*, pages 501–509, 2019.
- [34] Richard Zhang, Phillip Isola, and Alexei A Efros. Colorful image colorization. In *European Conference on Computer Vision*, pages 649–666. Springer, 2016.
- [35] D2B. D2BATK. <https://github.com/d2battack/D2BATK>, 2020.
- [36] Weilin Xu, David Evans, and Yanjun Qi. Feature squeezing: Detecting adversarial examples in deep neural networks. In *Proceedings of 25th Annual Network and Distributed System Security Symposium (NDSS)*, 2018.
- [37] Nilaksh Das, Madhuri Shanbhogue, Shang-Tse Chen, Fred Hohman, Li Chen, Michael E. Kounavis, and Duen Horng Chau. Keeping the bad guys out: Protecting and vaccinating deep learning with JPEG compression. *CoRR*, abs/1705.02900, 2017. URL <http://arxiv.org/abs/1705.02900>.
- [38] Shengyuan Hu, Tao Yu, Chuan Guo, Wei-Lun Chao, and Kilian Q Weinberger. A new defense against adversarial images: Turning a weakness into a strength. In *Advances in Neural Information Processing Systems*, pages 1633–1644, 2019.

## 6 Appendix

### 6.1 Comparison of Two Barrier Loss Functions

Besides the polynomial barrier loss function, we have also tried a linear barrier loss  $\mathcal{L}_i(y_i^{\text{adv}}) = k\{\text{ReLU}[y_i^{\text{adv}} - (b \cdot \text{high} + (1 - b) \cdot y_i^{\text{nat}})] + \text{ReLU}[(b \cdot \text{low} + (1 - b) \cdot y_i^{\text{nat}}) - y_i^{\text{adv}}]\}$ . The coefficient  $b$  allows us to start applying (linear) penalty when the value approaches the boundaries. Empirically we set  $k = 1e6$  and  $b = 0.95$ .

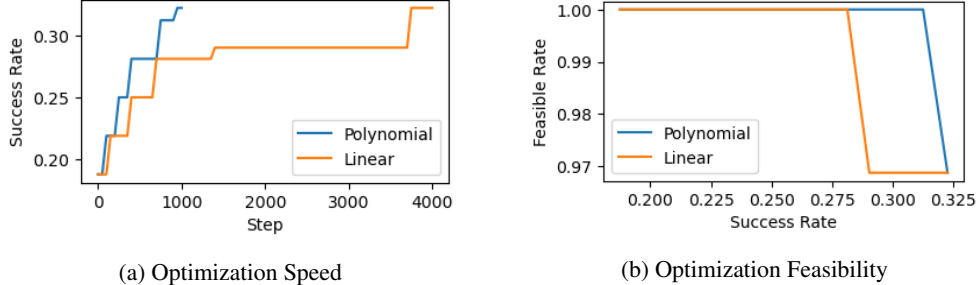


Figure 6: Comparison of two barrier loss functions. Graph (a) represents the success rate ( $y$  axis) after a given number of steps of optimization ( $x$  axis). Graph(b) represents for a given success rate ( $x$ ), how many examples have internal values within their boundary ( $y$  axis).

We observe that the linearly growing penalty is not strong enough to discourage bound violation even with a large  $k$  value. Figure 6 presents the polynomial barrier loss both converges faster and constrains the optimization better than the linear loss.

### 6.2 Comparing Optimization Methods

As discussed in Section 3.2, there are other optimization methods that can be used for our adversarial example generation such as two-step optimization and clipping. We conduct an experiment for those methods in comparison with our polynomial barrier method. The same optimizer, i.e., the Gradient Sign Method, is used for all the methods during evaluation. We use the adversarially trained ResNet152 model as our study subject. The throttle plane used in this evaluation is the plane before the shortcut sum operation in the last layer of Block 2. We use a bound of 1% of the difference between the minimum and maximum activation values, which are computed on the entire training dataset. Here, we use a value bound instead of a quantile bound to make different optimization methods comparable. For the two-step optimization method, we set the number of iterations to 100. At each iteration, we first optimize the internal values once and then the input ten times. We set the step size to 10% of the internal boundary for the internal optimization, and  $2.6e-3 \times 255$  for the input optimization. This optimization setting is similar to that in the paper [26]. For the clipping method, we optimize for 1000 iterations, and at each iteration we update the input once using the step size of  $2.6e-3 \times 255$ . For our algorithm, we run 1000 iterations with the step size of  $6.2e-3 \times 255$ .

Table 5: Comparison of optimization methods.

Method	Boundary		Consistency	Success Rate
	Feasibility	Average Size		
<b>Polynomial Barrier Method</b>	<b>97%</b>	<b>91%</b>	<b>Yes</b>	<b>25.8%</b>
Two-step Optimization	0%	204%	No	21.9%
Clipping	0%	429%	No	21.9%

Table 5 illustrates the results. Feasibility denotes the percentage of samples remaining in boundary after the optimization. Average size denotes the average boundary size of all the samples. We calculate the size using the equation  $\max_{i \in \mathcal{I}} \left[ \frac{\text{ReLU}(y_i^{\text{adv}} - y_i^{\text{nat}})}{\text{high} - y_i^{\text{nat}}} + \frac{\text{ReLU}(y_i^{\text{nat}} - y_i^{\text{adv}})}{y_i^{\text{nat}} - \text{low}} \right]$ . Consistency denotes if

the target internal values can be produced in the *original model*. Note that these optimization methods insert additional operations (e.g., clipping) that essentially change the dataflow of the original model. An observed internal value in the optimizing model may not be feasible in the original model. Success rate measures the percentage of generated samples that successfully induce misclassifications. It can be observed that most samples are still feasible after our optimization, while the other two methods cannot enforce the bound. Note that even though the clipping method clips internal values and suppresses gradients, updates on the input can still induce internal values that go beyond bound. The average boundary size of our method is much smaller than the other two, indicating that our barrier loss function can effectively enforce the bound. Adversarial samples generated by the other two methods are hence much less natural-looking. For consistency, we observe that the two baseline methods do not have any guarantee. As the subject model is adversarially trained and the internal bound is very tight, the attack is difficult to succeed. Nonetheless, our method still outperforms the baselines regarding the attack success rate.

### 6.3 Feature Smoothing

Occasionally, we observe the generated adversarial examples exhibit checkerboard patterns. Figure 7(a) shows a typical adversarial example with checkerboard pattern (zoomed in on the right). We observe these cases often occur when we attack VGG model but not ResNet152. We speculate that this is because we enforce bounds for individual values (on a throttle plane) independently and do not consider their joint distribution of nearby neurons. To mitigate the problem, we add a feature smoothing loss to the optimization goal. The intuition is that individual values (on a plane) have a similar trend of change with their neighboring values. Thus we calculate the average of surrounding changes and use a mean squared error loss to prevent the change from being too far away from the average. Suppose  $y \in \mathbb{R}^{D \times H \times W}$  denotes a throttle plane with channel  $D$ , height  $H$  and width  $W$ . The quantile changes are written as  $\Delta Q_{d,h,w} = |C_{d,h,w}^{-1}(y_{d,h,w}^{\text{adv}}) - C_{d,h,w}^{-1}(y_{d,h,w}^{\text{nat}})|/\epsilon$ . The average of changes made to nearby values can be formulated with an average pooling operation  $\text{AvgPool}_{3 \times 3}(\Delta Q)$ . Thus we expect the smoothness loss, written as  $\frac{\alpha}{D \cdot H \cdot W} \sum_{d,h,w} [\text{AvgPool}_{3 \times 3}(\Delta Q)_{d,h,w} - \Delta Q_{d,h,w}]^2$  to be small. We empirically set the weight of smooth loss to  $\alpha = 10$ . This can lead to 6% improvement on the human preference rate for VGG16. After adding the smoothness loss, the checkerboard pattern is largely eliminated as shown in Figure 7(b).

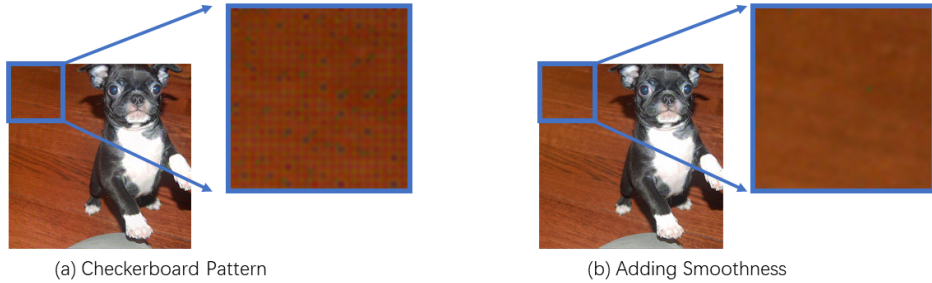


Figure 7: Results before and after smoothing for a VGG16 model

### 6.4 Transferability of Generated Adversarial Examples

In this section, we study the transferability of adversarial examples generated by different attacks. We launch untargeted attacks on ResNet152-Adv and targeted attacks on ResNet50. We use the same attack success criterion as in Section 4.1: (1) targeted adversarial examples should induce the same target label when transferred to a second model; (2) untargeted adversarial examples should exclude the true label from appearing in the top-5 predicted labels when transferred. We test generated adversarial samples on 4 different models, including ResNet50' (with the same structure but different parameters as the previously used ResNet50), VGG19, MobileNet and DenseNet. The results can be found in Table 6 and Table 7. We observe that our untargeted attack has higher human preference than other attacks with comparable transferability. For targeted attacks, our method outperforms other methods in both transferability and human performance. Note that transferring targeted attack is a challenging task and requires specific approaches (e.g., ensemble) to improve the transferability.

Table 6: Transferability of untargeted attacks. Adversarial examples are generated on ResNet152-Adv model.

Attack	Transfer to				Human Preference
	ResNet50'	VGG19	DenseNet121	MobileNet-V1	
PGD-4	50/100	60/100	46/100	61/100	30%
FS1	43/100	51/100	39/100	52/100	35%
SM50	49/100	57/100	48/100	47/100	29%
D <sup>2</sup> B40	55/100	56/100	47/100	60/100	<b>41%</b>
D <sup>2</sup> B50	<b>67/100</b>	<b>63/100</b>	<b>57/100</b>	<b>70/100</b>	20%

Table 7: Transferability of targeted attacks. Adversarial examples are generated on ResNet50 model.

Attack	Transfer to				Human Preference
	ResNet50'	VGG19	DenseNet121	MobileNet-V1	
PGD-4	37/100	0/100	0/100	1/100	27%
FS1	17/100	<b>2/100</b>	0/100	<b>1/100</b>	36%
SM50	2/100	0/100	0/100	0/100	21%
SM500	32/100	0/100	<b>1/100</b>	0/100	14%
D <sup>2</sup> B100	<b>44/100</b>	0/100	0/100	0/100	<b>50%</b>

## 6.5 Binary Search for Optimization Step Size

In our adversarial example generation, a proper step size (learning rate) is crucial for reliable optimization. A small change on the input can lead to a large quantile change on an internal throttle plane, which makes the optimization oscillating and may even lead to numerical exceptions. Choosing an optimal step size depends on model structure and the selected throttle plane(s). It is impossible to manually preset a step size for all the cases. We hence leverage binary search to look for an appropriate step size.

Specifically, we first determine a possible search range for step size, e.g. [0, 255] for the gradient sign method on RGB values. We then choose the median value of the search range as a probing step size. We use this probing step size to conduct optimization for a given number of steps. If the internal quantile change goes beyond the boundary, it means the probing step size is too large for the optimization. We hence update the upper bound of the search range to the current probing value. Otherwise, we update the lower bound with the probing value. We repeat the above search procedure for a given number of iterations.

## 6.6 Differential Analysis - Understanding the Essence of D<sup>2</sup>B

In this experiment, we give D<sup>2</sup>B a very small internal bound, i.e., 5e-4% quantile change on the throttle plane of ResNet50. As such, the pixels changes enabled by the bound indeed are so small that they essentially denote the input gradients induced by our method. We also conduct a similar experiment for the pixel space BIM method (with approximately the same  $\ell_\infty = 2.77e-05 \times 255$ ) for reference. The results are presented in Figure 8, where the pixel differences between adversarial example and their original versions are presented. We observe that the “gradients” in pixel space attacks are more prevalent and uniform, whereas the “gradients” in our attack closely couple with the existing content features. Note that the experiment cannot be done on feature attack and semantic attack as there is no way to enforce a small bound for those attacks.

## 6.7 Choosing Throttle Planes

As we know, different layers represent features of various types, e.g., shallow layers for concrete features and deep layers for abstract features. For imperceptibility, a good idea is to simultaneously harness both concrete features (e.g. local textures) and abstract features (e.g. global outlines). Driven by this intuition, we use multiple throttle planes simultaneously instead of a single one. Guided by our

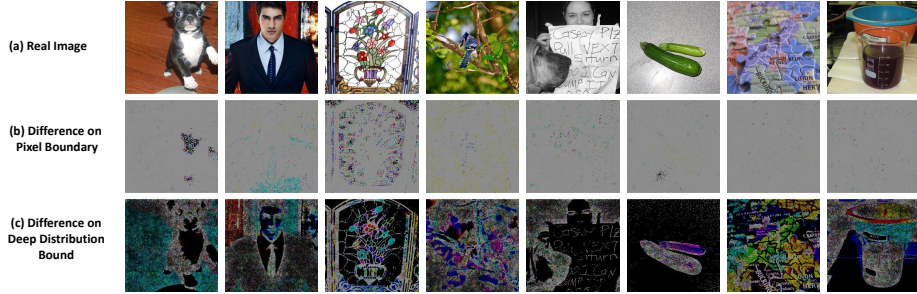


Figure 8: Differential Analysis. The first row denotes benign examples. The following two rows are pixel-wise differences between benign inputs and their corresponding adversarial versions. The second row is from BIM and the third row ours. Both have very small bounds. The differences are scaled up by a factor of  $2e6$  for the two respective rows for better display.

principle of looking for normal distributions, we check the normality of various layers in a model and identify a throttle plane list. We empirically choose three representative throttle planes for each model. We conduct the selection of the throttle planes for ResNet152-Adv and VGG16. The specific locations of throttle planes we choose can be found in the following Table 8, and the corresponding distribution samples from these chosen throttle planes can be found at Appendix 6.10. For models other than the aforementioned ones, we make use of a *proxy* method. Specifically, for a given benign input, we pass it to the subject model and also a *proxy model*, which is either ResNet152-Adv or VGG16 having well chosen throttle planes. The cross entropy loss is computed from the subject model whereas the barrier loss is computed from the proxy model, achieving using the proxy model internals to bound the changes while causing misclassification for the subject model. This leverages the observation that VGG and adversarially trained ResNet have good feature extraction and hence are more suitable for deep bounding. For the visual quality studies, we consistently used the throttle planes from VGG16.

Table 8: Chosen throttle planes for each model

Model	Plane 1	Plane 2	Plane 3
ResNet152-Adv	a. the first conv.	b. group 1	b. group 2
VGG16	a. conv1_2	a. conv2_2	a. conv3_3

Notation a. represents right after an operation. Notation b. represents the throttle plane which lies in the last block in the group and before the sum operation of the shortcut; conv. represents a convolution layer.

## 6.8 Evaluation on Different Models and Their Corresponding Distances

In this section, we evaluate D<sup>2</sup>B with different quantile changes on 4 models including DenseNet, MobileNet, VGG19 and ResNet50. We use the same setting as in Section 4.1. The results are shown in Table 9. We have similar observations as in Table 1 (Section 4.1). With a similar or higher level of attack confidence, our attack has a smaller  $\ell_2$  pixel distance and  $\ell_\infty$  quantile distance on all the three planes compared to BIM4. This indicates that our attack is more effective in bounding internal perturbations and can generate more natural-looking adversarial examples. We also observe that D<sup>2</sup>B induces a larger  $\ell_\infty$  pixel distance with a smaller  $\ell_2$  pixel distance compared to BIM4 at similar level of attack confidence, which indicates the piggy-backing nature of our attack.

Table 9: Targeted attacks on various models

Models	Attack	Confidence	Pixel Distance		$\ell_\infty$ Quantile Distance		
			$\ell_2$	$\ell_\infty$	Plane 1	Plane 2	Plane 3
MobileNet	BIM4	47.64	10.51	0.04	0.58	0.78	0.88
	D <sup>2</sup> B10	26.17	3.22	0.05	0.06	0.08	0.09
	D <sup>2</sup> B20	39.82	4.86	0.06	0.11	0.15	0.17
	D <sup>2</sup> B30	44.52	5.55	0.07	0.17	0.23	0.26
	D <sup>2</sup> B40	47.04	5.92	0.08	0.22	0.30	0.34
	D <sup>2</sup> B50	47.92	5.99	0.08	0.28	0.38	0.43
DenseNet	BIM4	49.21	10.68	0.04	0.59	0.81	0.89
	D <sup>2</sup> B10	20.60	3.48	0.05	0.06	0.08	0.09
	D <sup>2</sup> B20	41.14	5.74	0.08	0.11	0.16	0.17
	D <sup>2</sup> B30	50.94	6.81	0.09	0.17	0.24	0.26
	D <sup>2</sup> B40	56.33	7.45	0.10	0.23	0.33	0.35
	D <sup>2</sup> B50	60.10	7.93	0.11	0.29	0.40	0.44
VGG19	BIM4	56.64	12.13	0.04	0.68	0.88	0.97
	D <sup>2</sup> B10	-2.33	2.82	0.04	0.07	0.09	0.09
	D <sup>2</sup> B20	7.60	5.58	0.08	0.13	0.17	0.19
	D <sup>2</sup> B30	18.37	7.97	0.11	0.20	0.26	0.29
	D <sup>2</sup> B40	29.74	9.87	0.12	0.27	0.35	0.38
	D <sup>2</sup> B50	40.49	11.59	0.14	0.33	0.44	0.48
ResNet50	BIM4	81.91	10.81	0.04	0.62	0.83	0.90
	D <sup>2</sup> B10	30.29	4.26	0.07	0.06	0.08	0.09
	D <sup>2</sup> B20	58.82	6.27	0.09	0.12	0.16	0.17
	D <sup>2</sup> B30	72.43	7.28	0.10	0.18	0.24	0.26
	D <sup>2</sup> B40	80.06	7.88	0.11	0.24	0.32	0.35
	D <sup>2</sup> B50	84.52	8.25	0.11	0.30	0.41	0.44

## 6.9 Adversarial Examples of Different Scales

We show the generated adversarial examples using D<sup>2</sup>B with different settings in Figure 9 and Figure 10. Figure 9 demonstrates samples of a targeted attack on ResNet50 and Figure 10 an untargeted attack on ResNet152-Adv. We can observe that most of our adversarial examples are indistinguishable from real images (top row). For few cases such as the 3rd column in the last row (with large quantile change), we observe the presence of a repeating pattern. We speculate this is because the attack was only applied to the first a few representative throttle planes, which may not be as abstract as other deeper layers. This effect can be alleviated by including more throttle planes when launching the attack.

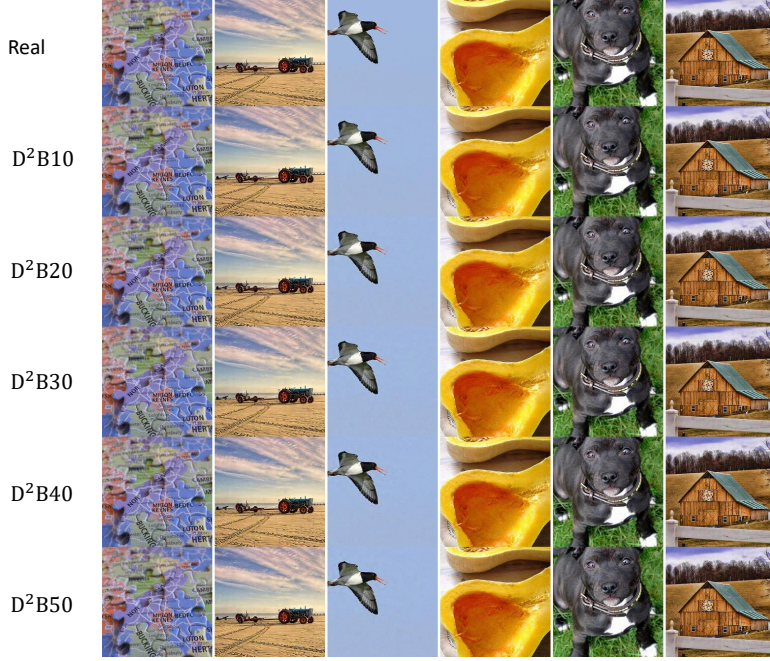


Figure 9: Adversarial Samples on ResNet50 of Different Scales

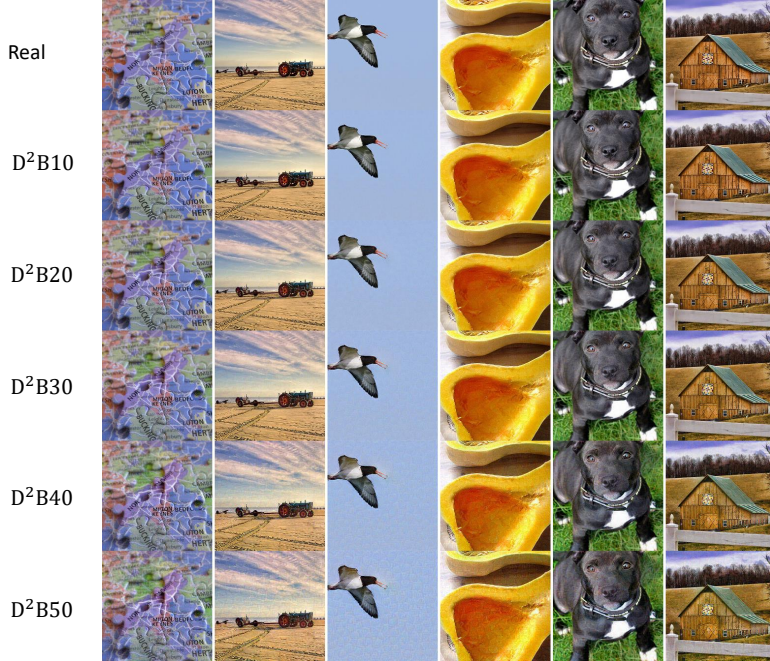
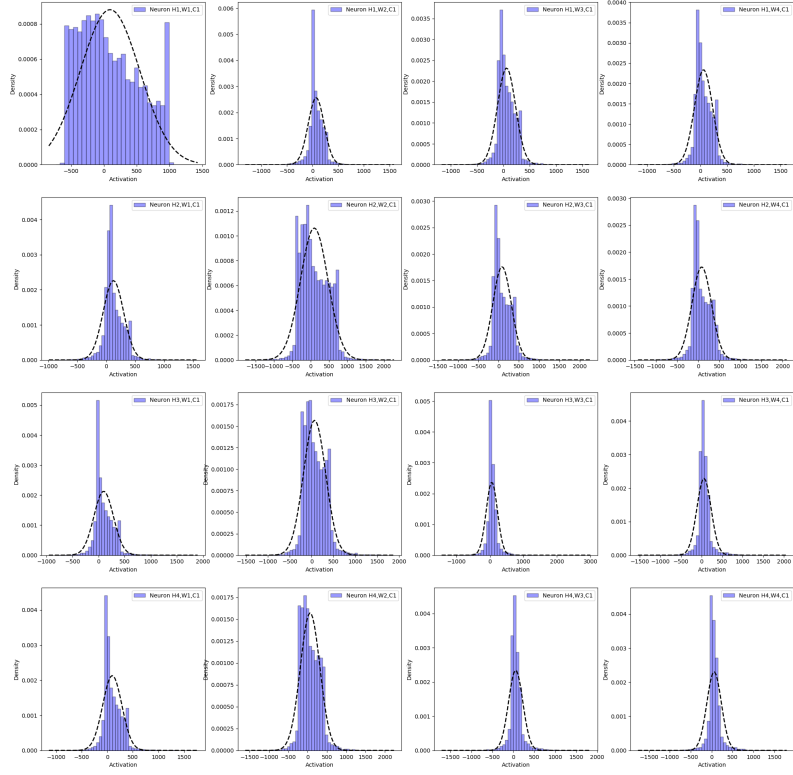


Figure 10: Adversarial Samples on ResNet152-Adv of Different Scales

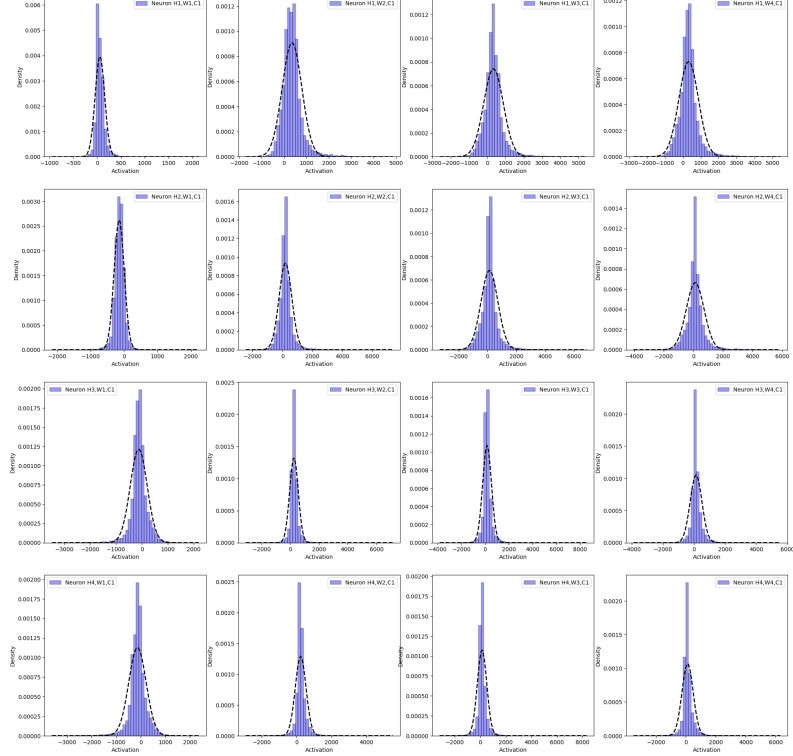
### 6.10 Typical Throttle Plane Distributions

We present some typical distributions from selected throttle planes in Figure 11 and Figure 12. Figure 11 shows distribution density graphs of  $4 \times 4 \times 1$  slice (width  $\times$  height  $\times$  channel) of selected throttle planes for VGG16, and Figure 12 for ResNet152-Adv. We observe that they have relatively different shapes and scales, which supports the choice of neuron specific bound in our attack. We also observe that activation distributions of deeper planes (e.g., Figure 11d and Figure 12e) more resemble a normal distribution. The first few rows and columns in Figure 11a and Figure 12a look less like a normal distribution. This is due to the existence of zero padding in those layers. The

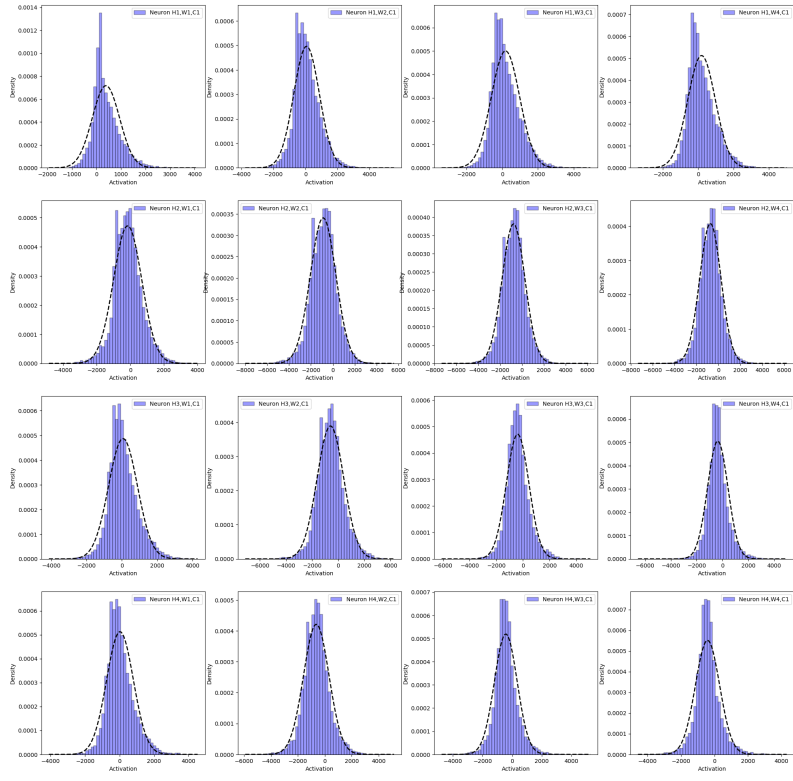
padding operation makes the first a few neurons around the border of a channel distinct from the inner neurons.



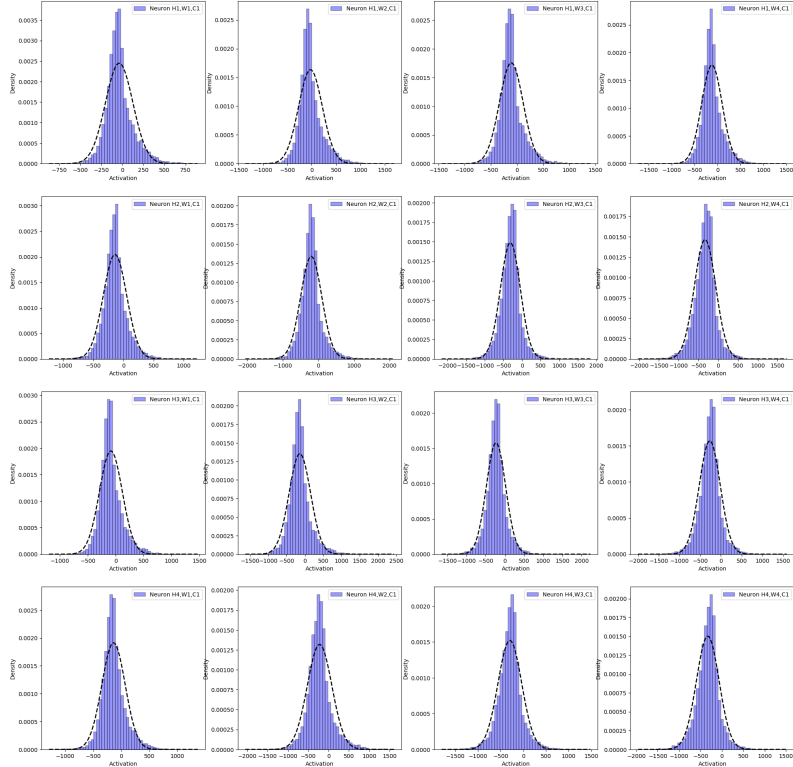
(a) Throttle Plane 1: After conv1\_2



(b) Throttle Plane 2: After VGG16 conv2\_2

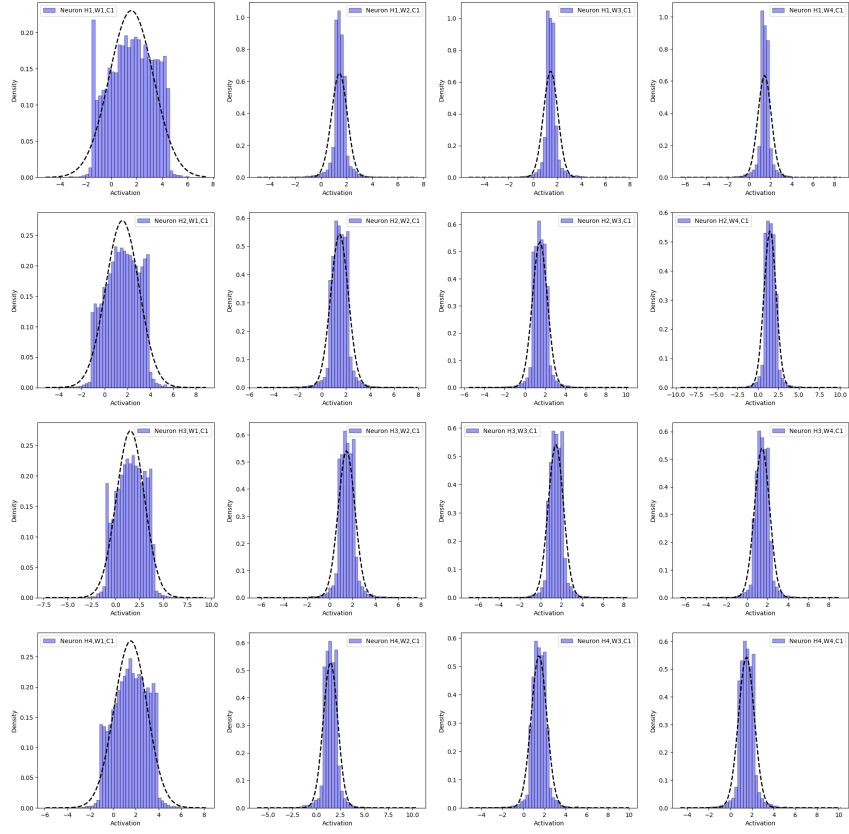


(c) Throttle Plane 3: After VGG16 conv3\_3

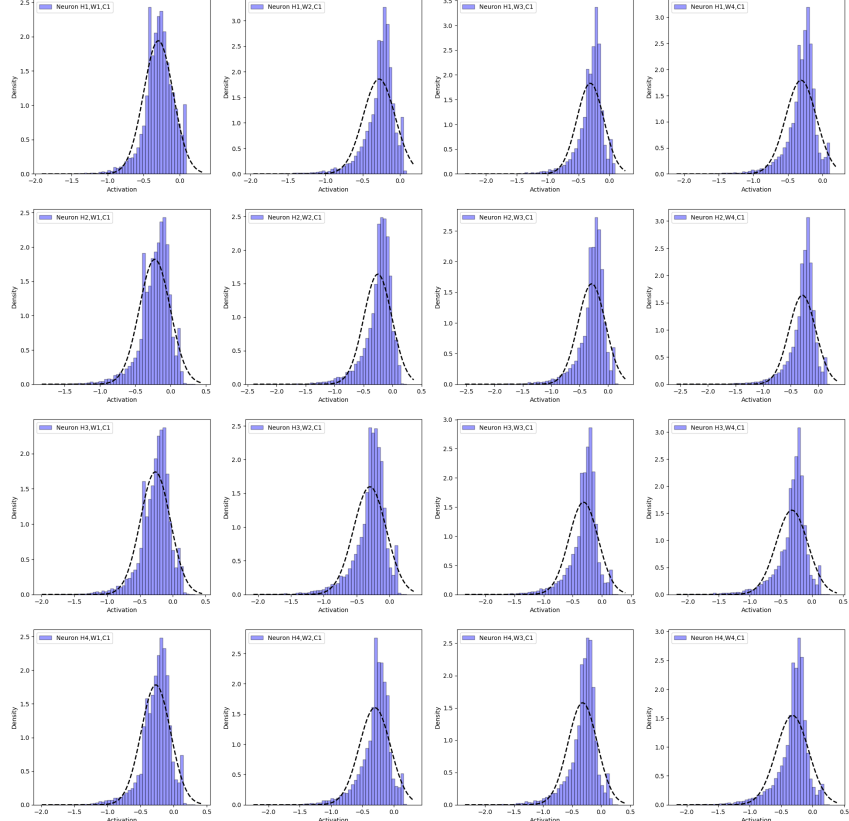


(d) Throttle Plane 4: After VGG16 conv4\_3

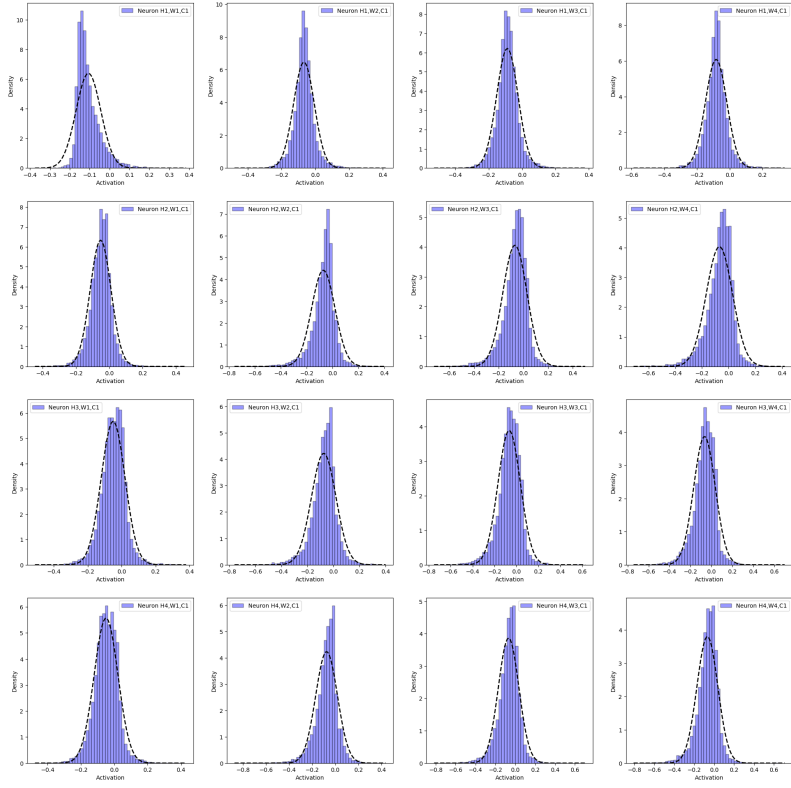
Figure 11: Typical Distributions of Selected Throttle Planes from VGG16



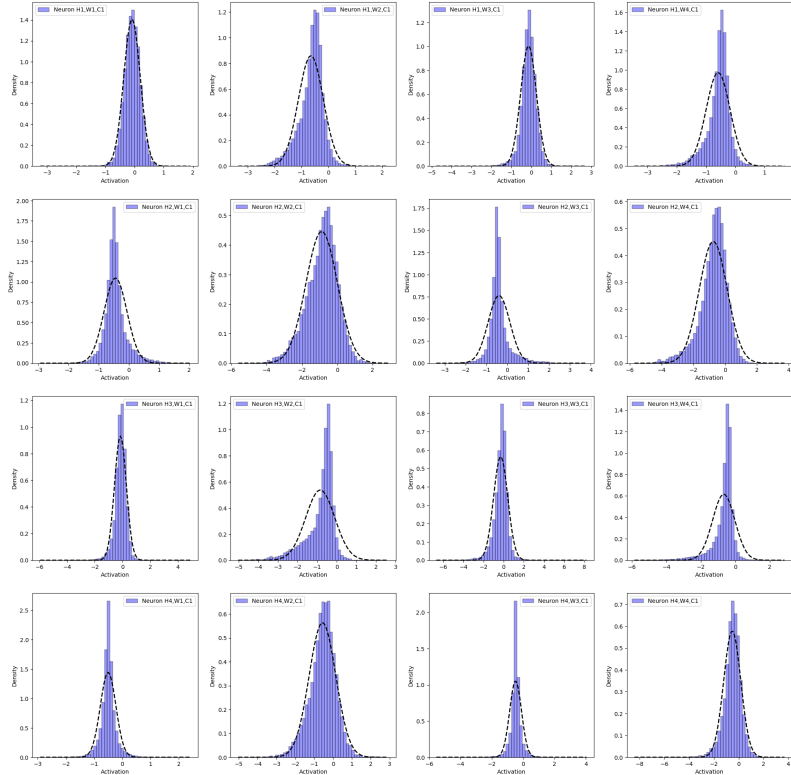
(a) Throttle Plane 1: After the First Convolution



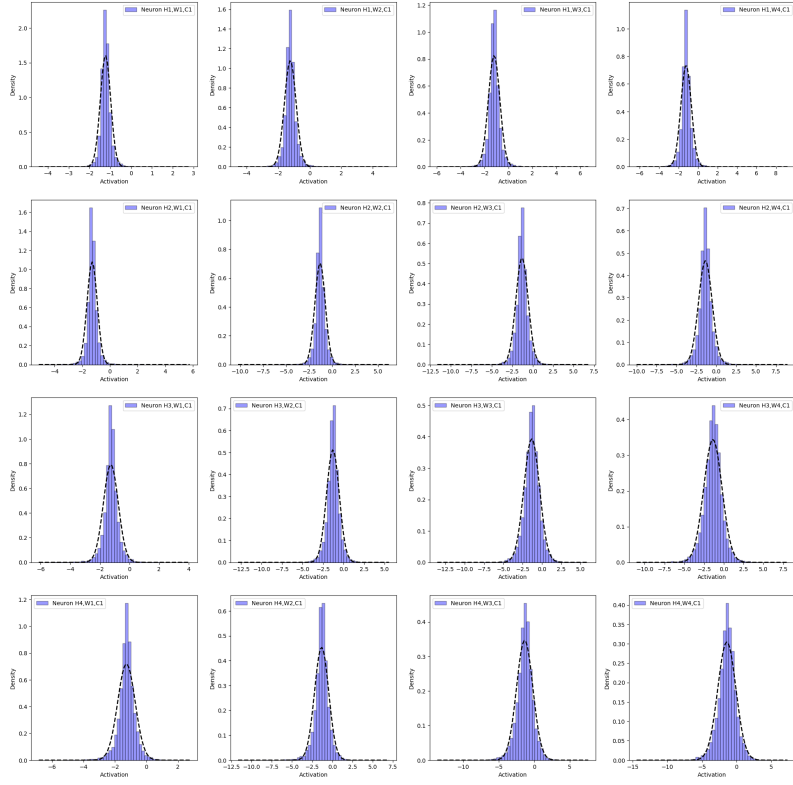
(b) Throttle Plane 2: Last Layer of Group 1 Before Sum



(c) Throttle Plane 3: Last Layer of Group 2 Before Sum



(d) Throttle Plane 4: Last Layer of Group 3 Before Sum



(e) Throttle Plane 5: Last Layer of Group 4 Before Sum

Figure 12: Typical Distributions of Selected Throttle Planes from ResNet152-Adv